Rapid and Noise-Resilient Mapping of Photogenerated Carrier Lifetime in Halide Perovskite Thin Films

Guillaume Vidon, Gabriele Scrivanti, Etienne Soret, Nao Harada, Emilie Chouzenoux, Jean-Christophe Pesquet, Jean-françois Guillemoles, Stefania Cacovich

ADVANCED FUNCTIONAL MATERIALS
www.afm-journal.de

Rapid and Noise-Resilient Mapping of Photogenerated Carrier Lifetime in Halide Perovskite Thin Films

*Guillaume Vidon, Gabriele Scrivanti, Etienne Soret, Nao Harada, Emilie Chouzenoux, Jean-Christophe Pesquet, Jean-François Guillemoles, and Stefania Cacovich**

Halide perovskite materials offer significant promise for solar energy and optoelectronics yet understanding and enhancing their efficiency and stability require addressing lateral inhomogeneity challenges. While photoluminescence imaging techniques are employed for the measurement of their opto-electronic and transport properties, going further in terms of precision requires longer acquisition times. Prolonged exposure of perovskites to light, given their high reactivity, can substantially alter these layers, rendering the acquired data less meaningful for analysis. In this paper, a method to extract high-quality lifetime images from rapidly acquired, noisy time-resolved photoluminescence images is proposed. This method leverages concepts of the field of constrained reconstruction and includes the Huber loss function and a specific form of total variation regularization. Through both simulations and experiments, it is demonstrated that the approach outperforms conventional pointwise methods. Optimal acceleration and optimization parameters tailored for decay time imaging of perovskite materials, offering new perspectives for accelerated experiments crucial in degradation process characterization are identified. Importantly, this methodology holds the potential for broader applications: it can be extended to explore additional beam-sensitive materials, and other imaging characterization techniques and employed with more complex physical models to treat time-resolved decays.

1. Introduction

Local quantitative luminescence analyses of semiconductor materials play a pivotal role in elucidating critical insights into both their intrinsic properties and their performance within devices.[1,2] These analytical techniques, which include optical microscopy and spectroscopic methods, offer a profound understanding of charge carrier recombination and transport phenomena, spanning a broad spectrum of length scales, from the micro to macro domains.[3] In particular, time-resolved photoluminescence analysis has emerged as a widely employed characterization method, serving as a powerful tool for investigating the complex dynamics of carriers within a semiconductor absorber.[4,5] It permits the quantification of key transport parameters, including carrier diffusion length, and surface or bulk recombination rates.[6–8] One critical physical parameter in semiconductor characterization is the carrier characteristic decay time, often denoted as carrier lifetime in the scientific literature. It is imperative to note that the term "*lifetime*" might be misleading, as it does not represent an intrinsic property of the material but it depends on several parameters related to the excitation such as laser fluence or repetition rate.[9] To prevent misinterpretation, it is thus crucial to clearly define this parameter within the specific experimental conditions. On a general basis, the assessment of local material properties remains a substantial challenge due to the inherent limitations arising from the low signal-to-noise ratio (SNR) of individual pixels when using imaging techniques.

Numerous physical models have been proposed to quantitatively assess and differentiate the location of non-radiative recombination within a semiconductor.[10–13] Specifically, these models seek to distinguish the bulk lifetime (τ_{bulk}) from the surface recombination rate (S_{top}). In this work, we have adopted a model based on the work of Gaubas and colleagues,[14] adapting it for an intrinsic semiconductor and applying it to imaging methods.[15] This method stands out as a powerful tool that eliminates the need for conducting multiple experiments involving varying laser power[16–18] or excitation wavelengths[19,20] to determine bulk and surface recombination rates. In the pursuit of addressing these limitations, our approach extends beyond

G. Vidon, E. Soret, J.-F. Guillemoles, S. Cacovich
Institut Photovoltaïque d'Ile-de-France (IPVF), UMR 9006, CNRS, Ecole Polytechnique, IP Paris, Chimie Paristech
PSL
Palaiseau 91120, France
E-mail: stefania.cacovich@cnrs.fr
G. Scrivanti, E. Chouzenoux, J.-C. Pesquet
Inria, CentraleSupélec, CVN
Université Paris-Saclay
3 Rue Joliot Curie, Gif-Sur-Yvette 91190, France
N. Harada
IPVF
Institut Photovoltaïque d'Ile-de-France
Palaiseau 91120, France

The ORCID identification number(s) for the author(s) of this article can be found under https://doi.org/10.1002/adfm.202402343

DOI: 10.1002/adfm.202402343

conventional methodologies by integrating regularization techniques into the analysis of low-fluence decay images. The necessity to operate at low fluences (i.e., with a carrier density of 10^{15} cm^{-3}, the expected carrier density of 1 sun equivalent illumination[21]) is an essential condition as it is representative of the operating conditions of a solar cell.

Moreover, reducing acquisition time and limiting the number of experiments is essential when investigating beam-sensitive materials,[22] such as organic semiconductors[23] or hybrid perovskite thin films and devices. Indeed, the interaction of lasers,[24] X-ray sources,[25,26] or electron beams[27,28] where the sample can cause temporary or permanent changes in fragile materials. The active layers of the current state-of-the-art perovskite solar cells exhibit notable spatial heterogeneity.[29] This non-uniformity in the composition of the absorber is a feature shared with other materials in the solar photovoltaic field, such as Copper Indium Gallium Selenide (CIGS).[30] However, perovskite materials stand out due to their unique characteristic of ion motion occurring at the timescale of tens of minutes and at scales of approximately one micron, both laterally[31–33] (x, y) and in-depth (z-axis).[34,35] This ion motion is related to electrochemical reactions involving components within the perovskite layer, interactions with the surrounding atmosphere, exposure to light, and interactions with neighboring layers. This dynamic behavior leads to phenomena like self-healing[36,37] and light soaking.[38,39]

To obtain more precise imaging, a common strategy involves averaging out noise by repeating experiments over extended periods of time. However, as previously noted, this can potentially induce modifications in the layer under examination. An alternative method is to enhance signals by increasing excitation power. Nevertheless, not only does this amplify chemical reactions but also induces a shift in the response regime of the layers—from a linear response to more intricate and complex behaviors. Therefore, methods to eliminate noise after the acquisition are needed.

In that regard, post-processing data treatment may significantly help in recovering local information on noisy datasets,[40] allowing the identification of new features in the reconstructed maps[41] by fitting physical models that contain a description of the noise statistics. With this aim, several approaches have been used in the literature to treat multidimensional datasets and extract local chemical or physical information, ranging from Principal Component Analysis[42,43] to variational regularization models.[44] At the core of this second group of approaches is the idea of minimizing a function that is defined as the combination of two fundamental elements: a *data fidelity term*, which controls the fitting of the modeled data to the measured ones, and a regularization term which encompasses the available a priori information on the sought-for solution. Among the most common forms of regularization, we mention *Tikhonov regularization*,[45] *Sparse Regularization*, and *Total Variation regularization*.[46] Moreover, in the field of fluorescence analysis, which is extensively used in biological studies, alternative approaches for handling lifetime maps have recently been proposed. These include leveraging Gaussian process priors,[47] adopting a Bayesian nonparametric (BNP) framework,[48] or employing faster photon counting methods.[49]

In this study, we integrate cutting-edge time-resolved luminescence imaging techniques with physical modeling and a specific form of total variation regularization to extract high-quality local maps of decay times on beam-sensitive materials. The methodology is validated on synthetic datasets and applied to various experimental datasets. Notably, our framework allows for the acquisition of high SNR images, even in the context of fast acquisitions. To demonstrate the versatility of our technique, we employ different acquisition times, leading to varying levels of noise. In summary, this paper makes two primary contributions. The first introduces an experimental technique enabling the acquisition of data cubes with high SNR images, albeit with extended experimental durations. The second contribution involves the introduction of a fitting and regularization framework. This framework facilitates rapid experimental acquisition while ensuring the recovery of data cubes with high SNR. Additionally, it enables the mapping of key physical parameters, offering a robust method for extracting meaningful information from rapidly acquired experimental data.

2. Results

2.1. Experimental Setup and Frameworks

We first present the time-resolved fluorescence imaging (TR-FLIM) acquisition technique, and how we adapted it to obtain high SNR acquisitions. In **Figure 1a**, we describe the experimental TR-FLIM setup employed for spatially time-resolved data acquisition.[50] The illumination source is a 532 nm pulsed laser. To ensure uniformity, the laser light undergoes homogenization through a rotating diffuser, effectively mitigating laser speckle. Lenses are used to de-collimate the laser, enabling wide-field illumination. Subsequently, the laser light passes through a beam splitter and an objective lens before reaching the sample. The emitted light from the sample is then imaged using the same objective lens. The laser reflection is filtered out, allowing only the photoluminescence (PL) to reach the TR-FLIM camera. The TR-FLIM camera is a gated camera, an imaging system that employs a gating mechanism to control time and capture images at specific time intervals within a repetitive experimental cycle.

The fact that the camera is gated allows us to keep the SNR of the acquisition high enough throughout the decay. Indeed, a gated camera allows for the selection of a time delay, t_{decay}, after each laser pulse, along with a gate width in the temporal domain, referred to as t_{gw}, during which a static image is recorded. As t_{decay} increases, there is a corresponding decrease in the light emission from the sample, giving rise to the term "decay". Throughout the study, the experimental SNR corresponds to the ratio between the mean value and the standard deviation of the values acquired throughout the t_{gw} at a specific t_{decay}, and it is expressed in arbitrary units (a.u.). An example of decay is presented in Figure 1b, where the x-axis is t_{decay}. If, a constant gate width is used for all the points of the decay, the decrease of the signal with t_{decay} leads to a concomitant reduction in the SNR. Therefore, to prevent that, we use for each point of the decay of Figure 1b, a different gate width, meaning that each point corresponds to a different value of t_{gw}. A second factor denoted here as experimental time, t_{exp}, can be tuned to reach high SNR even for points of decay with low signal. Indeed, as previously mentioned, when working with fragile materials, it becomes crucial to take into account the total duration of the experiment. Therefore, this experimental approach involves

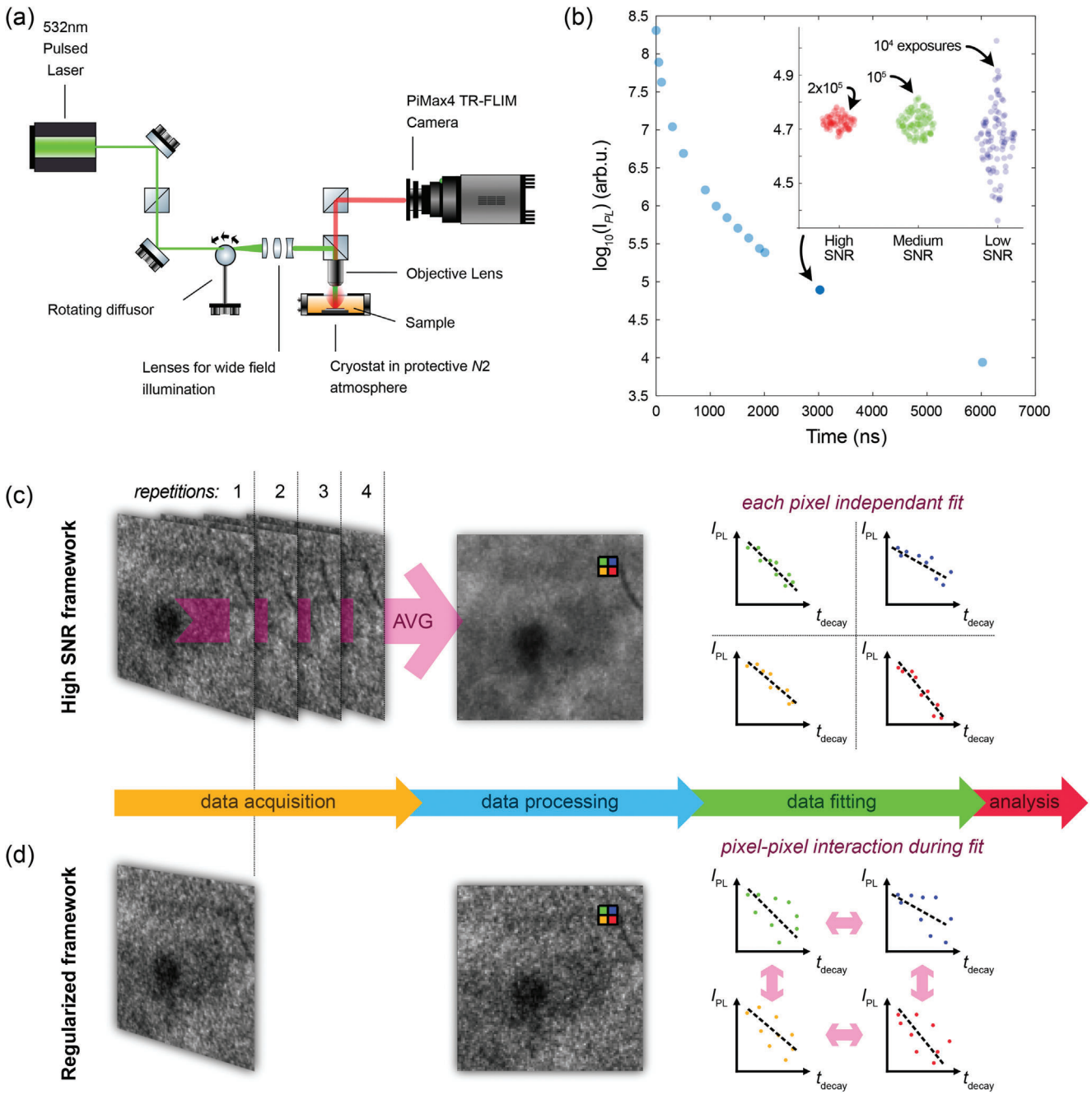

Figure 1. a) Schematic of the time-resolved fluorescence imaging set-up employed in this study. b) Decay averaged at a specific *x*–*y* location and at different times after the laser pulse (blue dots). For $t = 3000$ ns, the differences between high, low, and medium SNR are shown in the inset. They correspond to a change in the number of exposures per frame, set at 10 000, 100 000, and 200 000 for the low, medium, and high SNR acquisitions, respectively. c) High SNR framework depiction with data acquisition, data processing, and model fitting. In this framework, multiple repetitions are averaged out in order to obtain a smooth high SNR set of images. The individual decay of each pixel is then independently fitted. d) Regularized framework. In this framework, less experimental time is required but the fitting procedure involves pixel–pixel interaction.

two distinct but parallel temporal axes, the decay time t_{decay}, and the experimental time t_{exp}.

One of the key parameters of a gated camera is the number of repetitions of an acquisition. The impact of increasing repetitions is displayed in the inset of Figure 1b, where we varied the number of exposures per captured frame, showing the local decay for a small matrix of 2×2 pixels. In particular, we consider three different numbers of exposures at $t_{decay} = 3000$ ns. High SNR corresponds to 2×10^5 exposures per frame (red dots), medium SNR to 10^5 (green dots), and low SNR to 10^4 (blue dots). As expected, a higher number of exposures leads to a narrower distribution of the photoluminescence intensity values. We note that the

average value of the low SNR points is slightly lower than that of the high and medium SNR points—a pattern that we attribute to a camera artifact to date. A study of the SNR for each time delay for the three experimental conditions is reported in Table S2 (Supporting Information). The high SNR framework enables accurate layer characterization but entails a prolonged acquisition time, typically around $t_{exp} = 20$ min per data cube. More details on the exact procedure are provided in the Supporting Information.

Therefore, we are able to tune the experiments to obtain higher SNR at the cost of having longer experiments. However, the samples might react and thus evolve during such a long experimental time $t_{exp,}$ potentially introducing artifacts in the measurements. Additionally, long acquisition time prevents accessing the evolution of physical parameters occurring within this time scale, for instance during *operando* studies where real-time analysis is required. Those reasons pushed us to search for an alternative acquisition framework that could be used to monitor *fast* evolutions.

We thus conducted a comparative analysis of two frameworks, as sketched in Figure 1c (high SNR framework) and Figure 1d (regularized framework). Each framework comprises three distinct stages: i) data acquisition, characterized by a specific t_{exp}; ii) data processing, wherein all exposures per frame are averaged; and iii) model fitting to the experimental data, yielding outcomes such as lifetime maps. The principal difference between the two frameworks lies in the reduced t_{exp} in the case of a regularized framework. The achievement of such reduction is obtained through the incorporation of post-processing data analysis, based on data modeling and total variation regularization methods. In the following sections, we apply and compare the two frameworks on both simulated and experimental datasets.

2.2. Data Modeling

The simplest model that can be used to interpret a decay is based on a mono-exponential law.[51,52] At a certain time after the laser impulse, the evolution of the time-resolved photoluminescencethe intensity (P_i) for every pixel $i \in \{1, \dots, n\}$ can be approximated as a function of time by the exponential decay model

$$P_i(t) = \delta_i \, e^{\left(-\frac{t}{\tau_i}\right)} \tag{1}$$

where $\delta = (\delta_i)_{1 \le i \le n}$ is the set of pre-exponential factors and $\tau = (\tau_i)_{1 \le i \le n}$ is the set of lifetime values, which is referred to as the "lifetime map". This model is classically transformed into a linear one by taking the logarithm of the equation above:

$$\bar{p}_i(t) = a_i + b_i t \tag{2}$$

where $\mathbf{a} = (a_1, \dots, a_n) \in \mathbb{R}^n$, $\mathbf{b} = (b_1, \dots, b_n) \in \mathbb{R}^n$, $\bar{\mathbf{p}} = (\bar{p}_1, \dots, \bar{p}_n) \in \mathbb{R}^n$ and for every $i \in \{1, \dots, n\}$ we define $\bar{p}_i(t) = \log(P_i(t))$, $a_i = \log(\delta_i)$ and $b_i = -1/\tau_i$.

To work with a simpler model, we assume that the PL data measured during the k-th acquisition window, or "gate", $[t_k, t_k + \Delta_k]$ are acquired at a *single* instant t_k for every $k \in \{1, \dots, T\}$.

For every pixel $i \in \{1, \dots n\}$, P_i^k represents the mean intensity value of the acquisitions at pixel i over the acquisition window $[t_k, t_k + \Delta_k]$

$$P_i^k = \frac{1}{\Delta_k} \int_{t_k}^{t_k + \Delta_k} P_i(t) \, dt \tag{3}$$

In accordance with the notation introduced above, we define for every $k \in \{1, \dots, T\}$

$$p_i^k = \log\left(P_i^k\right) \tag{4}$$

and assuming that $\Delta_k \to 0$, the model described by Equation (2) reduces to the following discrete model for every $k \in \{1, \dots, T\}$ and for every $i \in \{1, \dots, n\}$

$$p_i^k = a_i + b_i t_k \tag{5}$$

We discuss the validity of this approximation in the Supporting Information. In a regular framework, each pixel is fitted independently as sketched in Figure 1c. This is the case in the high SNR framework presented above. On the contrary, in the case of the regularized framework, a link is introduced between neighboring pixels during the fitting stage, as shown in Figure 1d.

2.3. Principle and Description of the Regularization Framework

In the regularized framework, the fitting stage undergoes two primary changes: simultaneous fitting of all pixels and the integration of a regularization term into the model function. The so-called "fidelity" term gives the *price* of having the estimated and the experimental data far from one another. In order to reduce the sensitivity of the model to outliers, we adopt the robust Huber loss function[53] for the fidelity term, which is defined as follows:

$$(\forall u \in \mathbb{R}) \; H_\mu(u) = \begin{cases} \frac{1}{2\mu} u^2 & \text{if } |u| \le \mu \\ |u| - \frac{\mu}{2} & \text{otherwise} \end{cases} \tag{6}$$

where $\mu > 0$ can be adjusted according to the magnitude of the data. The data fidelity term is then expressed as:

$$\mathcal{F}(\mathbf{a}, \mathbf{b}) := \sum_{k=1}^{T} \sum_{i=1}^{n} H_\mu\left(p_i^k - a_i - t_k b_i\right) \tag{7}$$

Notably, the use of Huber's loss makes the model well-suited to the cases when the noise affecting the data corresponds to the realization of a Gaussian mixture model, which is a possible cause of outliers in the observed data.[54]

The second term is called the regularization term. The aim of this term is to use a priori *information* that we assume the model respects. The main assumption behind the regularization model is the following: the samples under study have a structure, and the local lifetimes are not randomly spatially distributed but do depend on the neighboring environment. Therefore, the lifetime of an individual pixel is expected to exhibit minimal variation in

comparison to the one of adjacent pixels. In addition, the components **a** and **b** (see Equation 2) should be correlated in terms of spatial information. Following this idea, we introduce a Structure Tensor Total Variation regularization function[55] (STV) in our fitting model: this function offers the advantage of effectively smoothing regular portions of the data while preserving sharp discontinuities within the image. As a result, piecewise constant images are included in the solution set. The regularization term is written as:

$$\left(\forall\,(\mathbf{a},\mathbf{b}) \in \mathbb{R}^{n\times 2}\right)\,\mathcal{R}\,(\mathbf{a},\mathbf{b}) = STV\,(\mathbf{a},\mathbf{b}) \tag{8}$$

Thus, the proposed regularized regression model is cast as a constrained optimization (minimization) problem in the spirit of the work of Combettes et al.,[56] where the cost function brings the estimated solution closer to the experimental data points and the constraint prevents too large variations inside the fitted map. We write it as:

$$\underset{(\mathbf{a},\mathbf{b})\in(\mathbb{R}^n)^2}{\text{minimize}}\,\mathcal{F}\,(\mathbf{a},\mathbf{b}) \;\text{ such that }\mathcal{R}\,(\mathbf{a},\mathbf{b}) \;\leq\; \eta \tag{9}$$

where $\eta > 0$ is an upper bound for the STV of the sought-for solution, which plays the role of a regularization parameter. Following the work in[57] we cast the problem as a convex non-smooth optimization problem and we address it by means of the Primal Dual optimization algorithm proposed in.[58,59] The technical details related to the definition of the STV regularization model and the optimization algorithm are included in the Supporting Information. Therefore, the regularized framework consists of using the proximity between neighboring pixels in order to reduce the number of repetitions required to get an interpretable lifetime image.

2.4. Proof of the Noise Tolerance on Synthetic Data

To prove that the regularized framework is tolerant to noise, we use simulated data onto which we add Gaussian noise of varying amplitude. It is important to note that the application of Huber's loss function can also be applied to noise models beyond Gaussian, but such extensions are beyond the scope of this study.

In this study, we use a physical interpretation model previously described in the literature by Gaubas and co-workers.[14] This method allows the estimation of both the bulk recombination coefficient τ_{bulk} and the top surface recombination velocity, referred to as S_{top}. The core concept behind this approach involves measuring the intercept, denoted as δ, of the long-time scale decay, as depicted in **Figure 2**a. This intercept, under certain hypotheses, can be employed to estimate S_{top}, thereby distinguishing between contributions from the bulk and the surface. However, in order to be able to quantify S_{top}, it is necessary to have previously determined the values of the diffusion coefficient D, of the sample thickness L and of the absorption coefficient α. Additional details about this model can be found in the Supporting Information.

First, synthetic data was generated using the drift–diffusion physical model, and an artificial imaging dataset was created, as shown in Figure 2b, to depict two different regions. These regions are distinguished by specific values of $\log(\delta)$ and τ (that correspond to different values of the drift–diffusion parameters). The central circle is characterized by $\log(\delta)$ and τ values of −0.77 (a.u.) and 117 *ns*, respectively. In contrast, the remaining square area exhibits $\log(\delta)$ and τ values of −2.15 (a.u.) and 197 *ns*. Then, different levels of additive Gaussian noise were added to the synthetic PL data, varying from 10^{-4} to 10^{-2}. In this simulation study, a wider range of noise values was tested in comparison to experimental data depicted in Figure 1, aiming to determine the "theoretical limits" of this approach with respect to noise tolerance. To validate our framework, we intend to extract the values of $\log(\delta)$ and τ fitted after the noise was added with our algorithm. As a quality metric of the fit, we use the sum of the normalized mean squared error (NMSE) between the estimated and the original data of the two components $\mathbf{a} \in \mathbb{R}^n$ and $\mathbf{b} \in \mathbb{R}^n$. The NMSE is a metric that assesses the accuracy of a regression model by measuring the average squared difference between the predicted and actual values, normalized by the mean of the actual values. In Figure 2c we report the NMSE obtained by the pointwise model (blue) and by the regularized model (orange) for five increasing levels of noise. On average, we gain one-half order of magnitude of precision in terms of NMSE with the regularized model as compared to the pointwise fitting. This means that it can be used to treat experimental data with higher levels of noise, for instance, obtained by performing faster experiments. Moreover, we compared against four additional frameworks involving the simple use of filters to assess their impact on noise reduction, specifically a Gaussian filter, a median filter, a non-local means filter and cubic smoothing splines. Notably, the regularized approach leads to lower values in terms of NMSE. This indicates that our proposed framework is the most effective method among the tested methods to treat this kind of multidimensional dataset, contributing to enhanced precision in the reconstruction of data.

We then report 1D profiles of the reconstructed synthetic data against their original configuration, both for the pointwise and the regularized model, to show the effect of the regularization on the solutions in Figure 2d,e for the two extracted parameters $\log(\delta)$ and $-1/\tau$. We observe that the regularized model performs better in estimating the mean values of the two regions and that it has a smaller variance around it, at least for the lowest levels of noise. For the two highest levels of noise (see Figure S4, Supporting Information), both the regularized and the pointwise models fail to estimate the original values, but the regularized model is still able to differentiate the two regions.

One key impact of the noise onto linear fitting is that it introduces correlations between the fitted slope and intercept, therefore, in the case under scrutiny, between the lifetime map and $\log(\delta)$ map. In Figure 2f–h we show this induced correlation on the artificial imaging dataset. This is illustrated as a 2D histogram where the $\log(\delta)$ values lie on the horizontal axis and the τ values on the vertical one. The color map illustrates the number of occurrences (pixels) of a certain $(\log(\delta), \tau)$ pair in the map. The original configuration is composed of two distinct regions, resulting in two correlation points in the $(\log(\delta), \tau)$ space, as shown in Figure 2f. In the correlation plot for the pointwise reconstruction (Figure 2g), the presence of noise in the simulated data makes the two points spread out one from the other, rendering their distinction difficult. However, with the solution obtained with the use of regularization, it is easier to distinguish two main correlation regions, as illustrated in Figure 2h, proving again that this approach results in a more accurate data reconstruction.

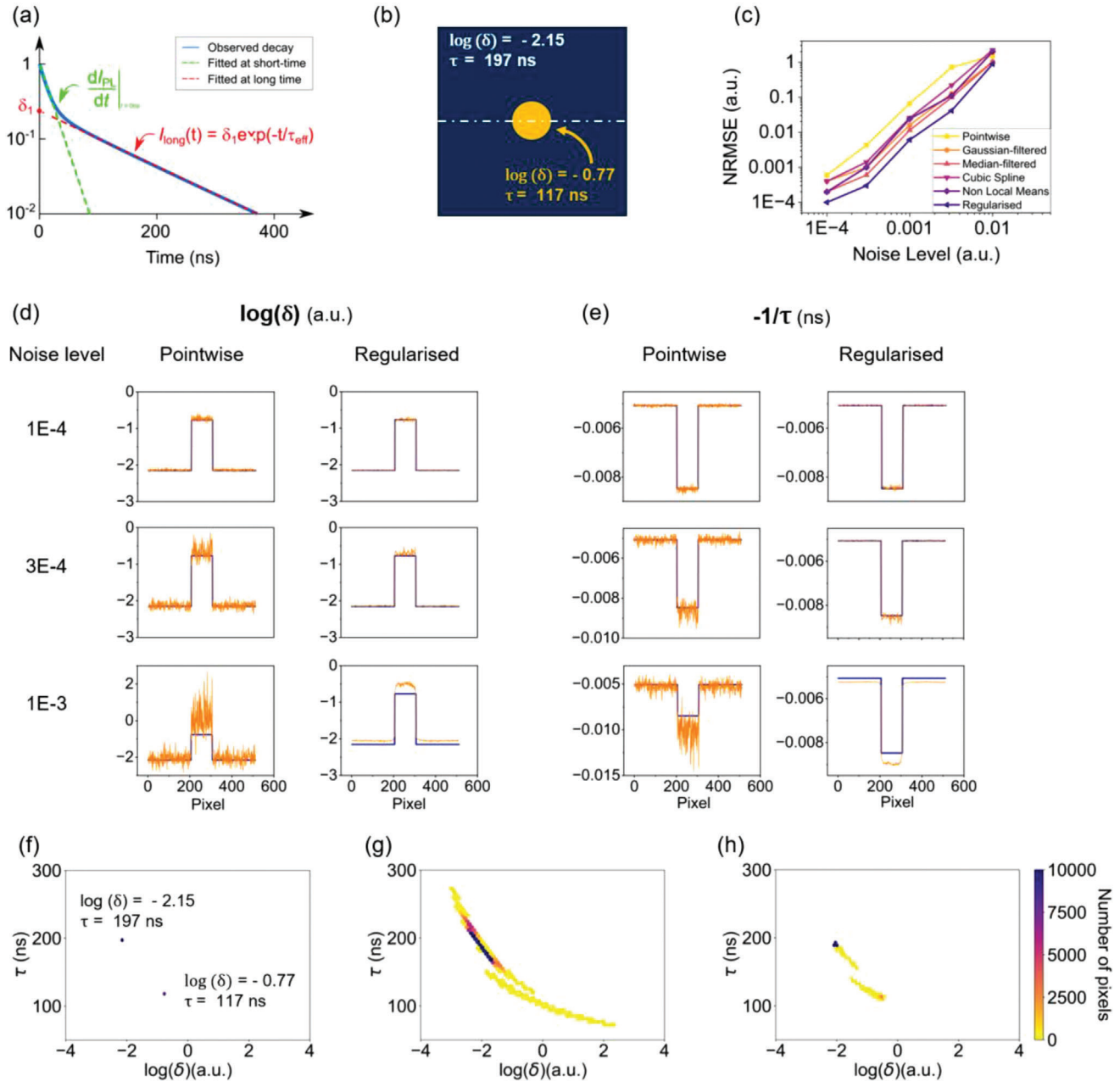

Figure 2. a) Sketch of the physical model employed for fitting time-resolved decays b) Synthetic dataset for $\log(\delta)$ and τ. c) Reconstruction error as a function of noise level for the pointwise and regularized algorithms and Gaussian, median, non-local means filters, and cubic splines. 1D profiles of the reconstructed synthetic data (blue lines) against the ground truth (orange lines) for $\log(\delta)$ and $-1/\tau$ for both pointwise d) and regularized e) data treatments. Each row corresponds to a different noise level (10^{-4}, 3×10^{-4}, and 10^{-3}). Correlation plots (expressed as 2D histograms) between the reconstructed $\log(\delta)$ (horizontal axis) and τ (vertical axis) on the simulated data set with noise level 0.001 for the synthetic data f), pointwise g) and regularized h) reconstruction.

2.5. Experimental Validation

We then validate our approach on experimental datasets, acquired with exposures per frame in the order of 10^4 (low SNR regime of Figure 1). The results are presented in **Figure 3**, wherein we compare the pointwise and regularized framework in terms of $\log(\delta)$ (Figure 3a,b) and lifetime maps (Figure 3d,e). The samples under investigation consist of double cations, double halide perovskites thin films, specifically $MA_{0.3}FA_{0.7}Pb(I_{0.84},Br_{0.16})_3$ which were deposited using a two-step evaporation/slot-die coating method as detailed in prior work.[60] We can observe the presence of local inhomogeneities on the samples, having the shape of globular structures. These might arise from a not uniform crystallization process over the

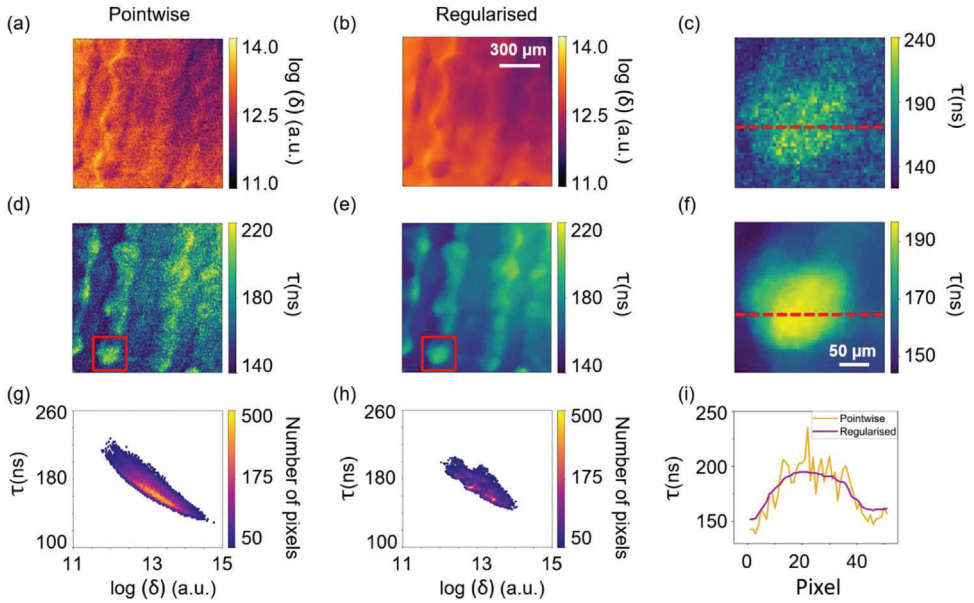

Figure 3. Maps of physical parameters extracted from experimental datasets. log(δ) maps of halide perovskite thin films reconstructed by pointwise a, b) regularized approaches. Lifetime maps reconstructed by pointwise d, e) regularized approaches. In c, f) a detail of pointwise and regularized lifetime maps, respectively are shown. Correlation plots (expressed as 2D histograms) between the reconstructed log(δ) (horizontal axis) and τ (vertical axis) on the simulated data set pointwise g) and regularized h) reconstruction. i) 1D profile of the lifetime maps (red line) shown in Figure 3c (pointwise) and Figure 3d (regularized).

substrates resulting in local differences in terms of thickness or chemical composition. However, determining their nature is beyond the scope of this work.

The introduced regularization model effectively mitigates noise in the estimated maps, particularly in the context of lifetime. This reduction in noise contributes to enhanced consistency among pixel values in neighboring regions. Additionally, the regularization model facilitates a higher level of discernible details. The heightened level of detail is particularly noteworthy when contrasted with pointwise reconstructions. To better evidence this aspect we show in Figure 3c,f the zoomed lifetime maps of one globular structure on the perovskite thin films, for a pointwise and regularized reconstruction, respectively. The 1D profile corresponding to the red dashed line is then reported in Figure 3i. We can notice a reduction of the noise along with an improved definition of the outline of the globular structure. Analogous to the approach adopted for synthetic data, we generated a plot illustrating the correlation between lifetime and log(δ) values for each pixel (Figure 3g,h). The results align with those observed in the simulation analysis, showing a more widely dispersed distribution in the case of pointwise reconstruction.

Finally, we compare the results of the two frameworks with the use of filters, applied after pointwise analysis. The log(δ), lifetime maps and correlation graphs between the two parameters are reported in Figure S5 (Supporting Information). While the application of filters actually improved the quality of the pointwise reconstructed images, the regularization still led to better results. Moreover, employing a regularized framework allows to directly integrate the a priori information into the fitting model and not just smoothing the final maps. In particular, the tensorial regularization we employed is designed to better promote the spatial consistency between the different channels of the data, representing a more rigorous, and probably less biased, approach to treat multi-dimensional datasets. These findings underline the efficiency of our proposed framework in improving the robustness and precision of lifetime and δ maps also on experimental datasets, thereby advancing the quality and reliability of time-resolved imaging analysis.

2.6. Influence of the Noise on Experimental Datasets

Moreover, to test the robustness of the regularization method, we explore the impact of changing the number of accumulations on experimental data in the same sample location, leading to acquisitions with different noise levels. In this case, we analyse a different sample, namely a formamidinium lead tri-iodide ($FAPbI_3$) perovskite thin film, deposited by flash infrared annealing.[61] In **Figure 4**a–c, we report the results of the pointwise method data treatment, while in Figure 4d–f we show the lifetime maps obtained with the regularized method. First, it is crucial to emphasize the lack of a ground truth for the experimental datasets. Moreover, a high number of repetitions may introduce additional artefacts in the time-resolved images. These artefacts could arise from factors such as the rotating diffuser or the camera itself. An example is the texture in the regularized high SNR (Figure 4c), a feature not detected through optical or electron microscopy characterization methods employed in the analysis of analogous samples in previous studies.[61] The reconstructed lifetime maps diverge significantly from each other with the pointwise approach. However, in the case of regularized lifetime maps, they exhibit remarkable similarity: in the case of a low-noise situation, the two frameworks coincide, as one would expect. In order to quantitatively gauge the similarity between the obtained lifetime maps,

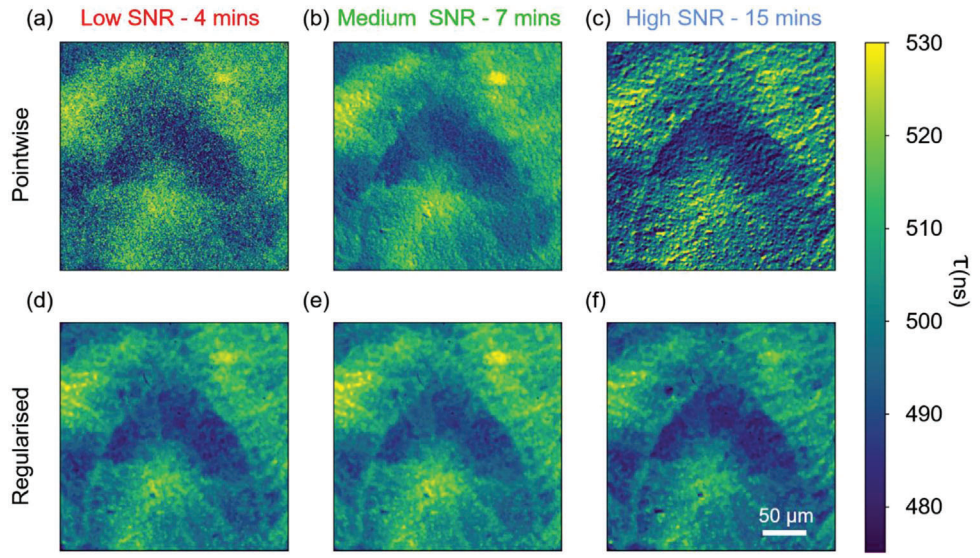

Figure 4. Pointwise a–c) and regularized d–f) lifetime maps for three maps acquired with different camera parameters. The variation of the camera parameters led to three levels of SNR, denoted as low, medium, and high corresponding to 4, 7, and 15 min of acquisition time, respectively.

we use the Root Mean Square Error (RMSE) and the Structure Similarity Index Measure (SSIM),[62] which provides a measure of the perceived change in structural information. SSIM takes into account three main components of perceived image quality: luminance, contrast, and structure. The SSIM index ranges between 0 and 1, with values close to 1 indicating high similarity. We highlight that the obtained figures do not provide a measure of the quality of the solutions, but only a quantitative assessment of the "closeness" of the lifetime maps we can estimate with the same method for different acquisition processes. Both for the computation of RMSE and SSIM, the values of the estimated lifetime maps were cropped between 470 and 540 ns and then linearly scaled to the interval [0,1] *ns*.

As illustrated in **Table 1** for the regularized maps and in **Table 2** for the pointwise maps, the estimated maps are more similar to each other (higher SSIM, lower RMSE) when the regularized approach is considered.

Table 1. SSIM (upper-left corner, underlined) and RMSE (lower-right corner, italic) scores between the regularized Lifetime maps.

	Low	Medium	High
High	0.795	0.919	
Low	0.859		1.7×10^{-4}
Medium		8.7×10^{-5}	1.2×10^{-4}

Table 2. SSIM (upper-left corner, underlined) and RMSE (lower-right corner, italic) scores between the pointwise Lifetime maps.

	Low	Medium	High
High	0.022	0.096	–
Low	0.06	–	3.7×10^{-4}
Medium	–	3.5×10^{-4}	4.6×10^{-4}

Moreover, in order to have a quantitative measure of over- and under-regularization and identify an optimal regularization parameter $\eta > 0$ in the absence of a reference distribution, we adopted the L-curve principle,[63,64] which was introduced in the case of Tikhonov regularization and then extended to Total Variation-based regularization models.[65–67] Further details and examples on this analysis can be found in the Supporting Information.

In this example, the effect of the regularization in improving the quality of the decay time maps is evident. This enhancement holds significant potential for refining the experimental design, as evidenced by a reduction in terms of acquisition time by a factor of more than three when going from low SNR maps (4 min) to high SNR maps (15 min). Furthermore, considering the good quality of the regularized low SNR maps, there is potential for additional reduction in acquisition time. These findings are particularly relevant in the case of beam-sensitive specimens or *operando* experiments, where it is crucial to distinguish the effects arising from the various aging conditions (temperature, atmosphere, illumination) from the possible damaging effects induced by the experiment itself.

3. Conclusion

In this work, we present a novel methodology for mapping the lifetime of semiconductor materials. Our approach integrates advanced photoluminescence time-resolved imaging analysis, modeling techniques, and the application of total variation regularization methods. This effectively mitigates local SNR limitations, granting access to a greater level of detail and features in the results. The analysis can be easily extended to determine the surface recombination rate, a parameter closely linked to δ. The determination of these key parameters can offer valuable insights into the advancement and optimization of halide perovskite materials. Indeed, the mitigation of bulk and interfacial recombination stands as a central focus within the solar cell

research community. This challenge, which has not yet been fully resolved, holds the potential to yield enhanced device efficiency and stability. Importantly, this approach can be further extended to precisely determine other physical parameters extracted from time-resolved analysis. These include mapping diffusion coefficient, carrier mobility, carrier diffusion length, radiative and non-radiative rates, as well as Auger recombination rates by employing more complex physical models. Moreover, our method offers the advantage of reducing the experimental acquisition time by at least a factor of three. This reduction is particularly noteworthy in the context of materials that are highly sensitive to beam exposure, such as absorbers utilized in various optoelectronic applications like halide perovskites or organic semiconductors. Consequently, our study not only contributes to the fundamental understanding of semiconductor behavior but also offers practical tools in the context of time-efficient data collection for the development of cutting-edge materials for optoelectronic applications. Finally, this method exhibits versatility in its applicability to *operando* experiments, facilitating the real-time monitoring and identification of degradation products arising from diverse ageing conditions.

4. Experimental Section

TR-FLIM Experimental Details: The Time-Resolved-FLuorescence IMaging (TRFLIM) setup recorded photoluminescence along three dimensions {*x*, *y*, time}. A Princeton Instruments PiMAX4 gated ultrafast camera was used. Photoluminescence decays were collected at different delays with gate time in the range of 3–7 ns. The illumination was performed with a Coherent Laser (λ = 532 nm, pulse width 15 ps), defocused, and homogenized on a 4.5 mm^2 area using a rotating diffuser to obtain a flat and homogenous wide field excitation. The repetition rate of the laser was set to 40 kHz. A × 10 objective or a ×100 objective was used both for excitation and collection, and the laser was filtered out with a DMLP605R beam splitter as well as with a FEL0610 filter.

$MA_{0.3}FA_{0.7}Pb(I_{0.84},Br_{0.16})_3$ Perovskite Deposition: The perovskite layer was deposited via a two-step evaporation/slot-die coating method.[60] In the first step, a 260 nm thick PbI_2 layer was evaporated at 3×10^{-7} mbar high vacuum pressure using MBraun-ProVap-5G equipment. Deposition rates were kept at 1 ± 0.1 Å s^{-1}. In the second step, the substrates with PbI_2 film were quickly transferred onto the slot-die coater (from nTact) for conversion. An organic solution containing 450 mg FABr, 290 mg FAI, 380 mg MAI, and 100 mg MACl prepared in 30 mL isopropanol (IPA) was pumped into the slot-die coating head with a constant dispense rate of 3.5 µL s^{-1}. The coating gap and the coating speed were kept at 60 µm and 2.5 mm s^{-1}, respectively. The organic solution infiltrated into the PbI_2 precursor film and reacted with it to form a wet perovskite film. To crystallize the perovskite, the substrates were annealed at 150 °C for 30 min. The final composition of perovskite was $MA_{0.3}FA_{0.7}Pb(I_{0.84},Br_{0.16})_3$.

$FAPbI_3$ Perovskite Deposition: The mixed A-cation hybrid perovskite precursor solution was deposited from a precursor solution containing FAI (1.2 M), PbI_2 (1.4 M), and CsI (0.21 M) in anhydrous DMF:DMSO (from Merck) 3:1 (v:v). All the organic salts were acquired from Greatcell Solar, while TCI provided lead halides and Merck provided DMSO and DMF solvents. The perovskite precursor solutions were deposited from a solution containing FAI and PbI_2 (1.5 M), in anhydrous DMF/DMSO 3:1 (v/v). The films made by the FIRA method included spin-coating of the perovskite solution in a single step at 4000 rpm for 10 s. The substrates were then IR irradiated with a 640 ms pulse in the FIRA oven, pulling them out immediately after the heating. The films were then placed onto a hotplate at 100 °C for 15 min to complete the solvent removal. FIRA processing was carried out in a glove box filled with an N_2 atmosphere.

Supporting Information

Supporting Information is available from the Wiley Online Library or from the author.

Acknowledgements

G.V. and G.S. contributed equally to this work. The authors thank Dr Van-Son Nguyen and Dr Sandy Sanchez for depositing the samples and Dr. Daniel Ory for fruitful discussions. Gabriele Scrivanti is a member of the Gruppo Nazionale Calcolo Scientifico-Istituto Nazionale di Alta Matematica (GNCS-INdAM) and thanks the ITN-ETN project TraDE-OPT funded by the European Union's Horizon 2020 research and innovation programme under the Marie Skłodowska-Curie grant agreement No 861137. This work represents only the authors' view and the European Commission is not responsible for any use that may be made of the information it contains. This project has been supported by the French Government in the framework of the program of investment for the future (Programme d'Investissement d'Avenir – ANR-IEED-002-01).

Conflict of Interest

The authors declare no conflict of interest.

Data Availability Statement

The data that support the findings of this study are available from the corresponding author upon reasonable request.

Keywords

carrier lifetime, halide perovskites, time-resolved photoluminescence imaging, total variation regularization

Received: February 6, 2024
Revised: March 12, 2024
Published online:

[1] T. Trupke, R. A. Bardos, M. C. Schubert, W. Warta, *Appl. Phys. Lett.* **2006**, *89*, 044107.
[2] X. Zheng, D. Kuciauskas, J. Moseley, E. Colegrove, D. S. Albin, H. Moutinho, J. N. Duenow, T. Ablekim, S. P. Harvey, A. Ferguson, W. K. Metzger, *APL Mater.* **2019**, *7*, 071112.
[3] G. Delport, S. Macpherson, S. D. Stranks, *Adv. Energy Mater.* **2020**, *10*, 1903814.
[4] R. K. Ahrenkiel, *Solid State Electron.* **1992**, *35*, 239.
[5] E. M. Hutter, T. Kirchartz, B. Ehrler, D. Cahen, E. von Hauff, *Appl. Phys. Lett.* **2020**, *116*, 100501.
[6] T. Kirchartz, J. A. Márquez, M. Stolterfoht, T. Unold, *Adv. Energy Mater.* **2020**, *10*, 1904134.
[7] L. Krückemeier, B. Krogmeier, Z. Liu, U. Rau, T. Kirchartz, *Adv. Energy Mater.* **2021**, *11*, 2003489.
[8] M. B. Johnston, L. M. Herz, *Acc. Chem. Res.* **2016**, *49*, 146.
[9] Y. Yuan, G. Yan, C. Dreessen, T. Rudolph, M. Hülsbeck, B. Klingebiel, J. Ye, U. Rau, T. Kirchartz, *Nat. Mater.* **2024**, *23*, 391.
[10] F. D. Heinz, W. Warta, M. C. Schubert, *Appl. Phys. Lett.* **2017**, *110*, 042105.
[11] G. Vidon, S. Cacovich, M. Legrand, A. Yaiche, D. Ory, D. Suchet, J.-B. Puel, J.-F. Guillemoles, *Phys. Rev. Appl.* **2021**, *16*, 044058.

[12] J. Warby, F. Zu, S. Zeiske, E. Gutierrez-Partida, L. Frohloff, S. Kahmann, K. Frohna, E. Mosconi, E. Radicchi, F. Lang, S. Shah, F. Peña-Camargo, H. Hempel, T. Unold, N. Koch, A. Armin, F. De Angelis, S. D. Stranks, D. Neher, M. Stolterfoht, *Adv. Energy Mater.* **2022**, *12*, 2103567.
[13] S. Eränen, M. Blomberg, *J. Appl. Phys.* **1984**, *56*, 2372.
[14] E. Gaubas, J. Vanhellemont, *J. Appl. Phys.* **1996**, *80*, 6293.
[15] G. Vidon, Why do decays decay? Transport and recombination dynamics of solar cells revealed via time resolved photoluminesence imaging: application to hybrid perovskites, Institut Polytechnique de Paris, Paris, **2022**.
[16] T. P. Weiss, B. Bissig, T. Feurer, R. Carron, S. Buecheler, A. N. Tiwari, *Sci. Rep.* **2019**, *9*, 5385.
[17] Y.-I. Ogita, *J. Appl. Phys.* **1996**, *79*, 6954.
[18] A. Buczkowski, Z. J. Radzimski, G. A. Rozgonyi, F. Shimura, *J. Appl. Phys.* **1991**, *69*, 6495.
[19] Y. Yang, Y. Yan, M. Yang, S. Choi, K. Zhu, J. M. Luther, M. C. Beard, *Nat. Commun.* **2015**, *6*, 7961.
[20] Y. Yang, M. Yang, D. T. Moore, Y. Yan, E. M. Miller, K. Zhu, M. C. Beard, *Nat. Energy* **2017**, *2*, 16207.
[21] R. Brenes, M. Laitz, J. Jean, D. W. deQuilettes, V. Bulović, *Phys. Rev. Appl.* **2019**, *12*, 014017.
[22] F. U. Kosasih, S. Cacovich, G. Divitini, C. Ducati, *Small Methods* **2021**, *5*, e2000835.
[23] J. B. Patel, P. Tiwana, N. Seidler, G. E. Morse, O. R. Lozman, M. B. Johnston, L. M. Herz, *ACS Appl. Mater. Interfaces* **2019**, *11*, 21543.
[24] H.-H. Fang, J. Yang, S. Tao, S. Adjokatse, M. E. Kamminga, J. Ye, G. R. Blake, J. Even, M. A. Loi, *Adv. Funct. Mater.* **2018**, *28*, 1800305.
[25] G. Vidon, P. Dally, M. Al-Katrib, D. Ory, M. Kim, E. Soret, E. Rangayen, M. Legrand, A. Blaizot, P. Schulz, J.-B. Puel, D. Suchet, J.-F. Guillemoles, A. Etcheberry, M. Bouttemy, S. Cacovich, *Adv. Funct. Mater.* **2023**, *33*, 2304730.
[26] S. Svanström, A. García Fernández, T. Sloboda, T. J. Jacobsson, H. Rensmo, U. B. Cappel, *Phys. Chem. Chem. Phys.* **2021**, *23*, 12479.
[27] C. Xiao, Z. Li, H. Guthrey, J. Moseley, Y. Yang, S. Wozny, H. Moutinho, B. To, J. J. Berry, B. Gorman, Y. Yan, K. Zhu, M. Al-Jassim, *J. Phys. Chem. C* **2015**, *119*, 26904.
[28] Z. J. W. A. Leijten, A. D. A. Keizer, G. de With, H. Friedrich, *J Phys Chem C Nanomater Interfaces* **2017**, *121*, 10552.
[29] K. Frohna, M. Anaya, S. Macpherson, J. Sung, T. A. S. Doherty, Y.-H. Chiang, A. J. Winchester, K. W. P. Orr, J. E. Parker, P. D. Quinn, K. M. Dani, A. Rao, S. D. Stranks, *Nat. Nanotechnol.* **2022**, *17*, 190.
[30] M. Krause, A. Nikolaeva, M. Maiberg, P. Jackson, D. Hariskos, W. Witte, J. A. Márquez, S. Levcenko, T. Unold, R. Scheer, D. Abou-Ras, *Nat. Commun.* **2020**, *11*, 4189.
[31] D. A. Jacobs, C. M. Wolff, X.-Y. Chin, K. Artuk, C. Ballif, Q. Jeangros, *Energy Environ. Sci.* **2022**, *15*, 5324.
[32] A. Bercegol, S. Cacovich, G. Vidon, S. Mejaouri, A. Yaiche, J.-B. Puel, C. Longeaud, J.-F. Guillemoles, S. Jutteau, J. Rousset, D. Ory, L. Lombez, *J. Phys. Chem. C* **2020**, *124*, 11741.
[33] T. Kim, S. Park, V. Iyer, B. Shaheen, U. Choudhry, Q. Jiang, G. Eichman, R. Gnabasik, K. Kelley, B. Lawrie, K. Zhu, B. Liao, *Nat. Commun.* **2023**, *14*, 1846.
[34] Y. Yuan, J. Huang, *Acc. Chem. Res.* **2016**, *49*, 286.
[35] S. Cacovich, L. Ciná, F. Matteocci, G. Divitini, P. A. Midgley, A. Di Carlo, C. Ducati, *Nanoscale* **2017**, *9*, 4700.
[36] D. R. Ceratti, Y. Rakita, L. Cremonesi, R. Tenne, V. Kalchenko, M. Elbaum, D. Oron, M. A. C. Potenza, G. Hodes, D. Cahen, *Adv. Mater.* **2018**, *30*, 1706273.
[37] V. Milotti, S. Cacovich, D. R. Ceratti, D. Ory, J. Barichello, F. Matteocci, A. Di Carlo, P. M. Sheverdyaeva, P. Schulz, P. Moras, *Small Methods* **2023**, *7*, e2300222.
[38] E. T. Hoke, D. J. Slotcavage, E. R. Dohner, A. R. Bowring, H. I. Karunadasa, M. D. McGehee, *Chem. Sci.* **2015**, *6*, 613.
[39] C. Zhao, B. Chen, X. Qiao, L. Luan, K. Lu, B. Hu, *Adv. Energy Mater.* **2015**, *5*, 1500279.
[40] K. Ji, W. Lin, Y. Sun, L.-S. Cui, J. Shamsi, Y.-H. Chiang, J. Chen, E. M. Tennyson, L. Dai, Q. Li, K. Frohna, M. Anaya, N. C. Greenham, S. D. Stranks, *Nat. Mach. Intell.* **2023**, *5*, 1225.
[41] M. Eom, S. Han, P. Park, G. Kim, E.-S. Cho, J. Sim, K.-H. Lee, S. Kim, H. Tian, U. L. Böhm, E. Lowet, H.-A. Tseng, J. Choi, S. E. Lucia, S. H. Ryu, M. Rózsa, S. Chang, P. Kim, X. Han, K. D. Piatkevich, M. Choi, C.-H. Kim, A. E. Cohen, J.-B. Chang, Y.-G. Yoon, *Nat. Methods* **2023**, *20*, 1581.
[42] J. Salmon, Z. Harmany, C.-A. Deledalle, R. Willett, *J Math Imaging Vis* **2014**, *48*, 279.
[43] S. Cacovich, F. Matteocci, M. Abdi-Jalebi, S. D. Stranks, A. Di Carlo, C. Ducati, G. Divitini, *ACS Appl. Energy Mater.* **2018**, *1*, 7174.
[44] J. Yang, W. Yin, Y. Zhang, Y. Wang, *SIAM J. Imaging Sci* **2009**, *2*, 569.
[45] J. B. Bell, *Math. Comput.* **1978**, *32*, 1320.
[46] L. I. Rudin, S. Osher, E. Fatemi, *Physica D* **1992**, *60*, 259.
[47] M. Fazel, S. Jazani, L. Scipioni, A. Vallmitjana, S. Zhu, E. Gratton, M. A. Digman, S. Pressé, *ACS Photonics* **2023**, *10*, 3558.
[48] M. Fazel, S. Jazani, L. Scipioni, A. Vallmitjana, E. Gratton, M. A. Digman, S. Pressé, *ACS Photonics* **2022**, *9*, 1015.
[49] J. E. Sorrells, R. R. Iyer, L. Yang, E. M. Martin, G. Wang, H. Tu, M. Marjanovic, S. A. Boppart, *ACS Photonics* **2022**, *9*, 2748.
[50] A. Bercegol, G. El-Hajje, D. Ory, L. Lombez, *J. Appl. Phys.* **2017**, *122*, 203102.
[51] J. Włodarczyk, B. Kierdaszuk, *Biophys. J.* **2003**, *85*, 589.
[52] S. Zhang, P. E. Shaw, G. Zhang, H. Jin, M. Tai, H. Lin, P. Meredith, P. L. Burn, D. Neher, M. Stolterfoht, *ACS Appl. Mater. Interfaces* **2020**, *12*, 37647.
[53] P. J. Huber, *International Encyclopedia of Statistical Science* (Ed.: M. Lovric), Springer, Berlin, Heidelberg, **2011**, p. 1248.
[54] E. Chouzenoux, J.-B. Fest, *J. Optim. Theory Appl.* **2022**, *195*, 919.
[55] B. Goldluecke, E. Strekalovskiy, D. Cremers, *SIAM J. Imaging Sci.* **2012**, *5*, 537.
[56] P. L. Combettes, J.-C. Pesquet, *IEEE Trans Image Process* **2004**, *13*, 1213.
[57] G. Chierchia, N. Pustelnik, J.-C. Pesquet, B. Pesquet-Popescu, *J. VLSI Signal Process. Syst. Signal Image Video Technol.* **2015**, *9*, 1737.
[58] L. Condat, *J Optim Theory Appl* **2013**, *158*, 460.
[59] B. C. Vũ, *Adv. Comput. Math.* **2013**, *38*, 667.
[60] V. S. Nguyen, I. Zimmermann, E. Grépin, K. Medjoubi, S. Jutteau, F. Donsanti, E. Bruhat, A. Duchatelet, S. Berson, J. Rousset, *Mater. Sci. Semicond. Process.* **2023**, *158*, 107358.
[61] S. Sánchez, S. Cacovich, G. Vidon, J.-F. Guillemoles, F. Eickemeyer, S. M. Zakeeruddin, J. E. K. Schawe, J. F. Löffler, C. Cayron, P. Schouwink, M. Graetzel, *Energy Environ. Sci.* **2022**, *15*, 3862.
[62] Z. Wang, A. C. Bovik, H. R. Sheikh, E. P. Simoncelli, *IEEE Trans Image Process* **2004**, *13*, 600.
[63] R. F. Ling, *J. Am. Stat. Assoc.* **1977**, *72*, 930.
[64] P. C. Hansen, *SIAM Rev.* **1992**, *34*, 561.
[65] X. Yang, R. Hofmann, R. Dapp, T. van de Kamp, T. dos Santos Rolo, X. Xiao, J. Moosmann, J. Kashef, R. Stotzka, *Opt. Express* **2015**, *23*, 5368.
[66] Y.-W. Wen, R. H. Chan, *IEEE Trans Image Process* **2012**, *21*, 1770.
[67] B. A. Tourn, J. C. Álvarez Hostos, V. D. Fachinotti, *Int. Commun. Heat Mass Transf.* **2021**, *125*, 105330.